OPTICA

Angle- and polarization-resolved luminescence from suspended and hexagonal boron nitride encapsulated $MoSe_2$ monolayers

Bo Han,[1] Sven Stephan,[1] Joshua J. P. Thompson,[2] Martin Esmann,[1] Carlos Antón-Solanas,[1] Hangyong Shan,[1] Nils Kunte,[1] Samuel Brem,[3] Sefaattin Tongay,[4] Christoph Lienau,[1,5] Kenji Watanabe,[6] Takashi Taniguchi,[7] Martin Silies,[1] Ermin Malic,[2,3] and Christian Schneider[1,5,*]

[1]Institute of Physics, Carl von Ossietzky Universität Oldenburg, Carl-von-Ossietzky-Straße 9-11, Oldenburg, 26129, Germany
[2]Department of Physics, Philipps-Universität Marburg, Renthof 7, Marburg 35032, Germany
[3]Department of Physics, Chalmers University of Technology, Gothenburg 412 96, Sweden
[4]School for Engineering of Matter, Transport, and Energy, Arizona State University, Tempe, Arizona 85287, USA
[5]Center for Nanoscale Dynamics (CeNaD), Carl von Ossietzky Universität Oldenburg, Carl-von-Ossietzky-Straße 9-11, Oldenburg, 26129, Germany
[6]Research Center for Functional Materials, National Institute for Materials Science, 1-1 Namiki, Tsukuba 305-0044, Japan
[7]International Center for Materials Nanoarchitectonics, National Institute for Materials Science, 1-1 Namiki, Tsukuba 305-0044, Japan
*Corresponding author: christian.schneider@uni-oldenburg.de

Received 19 May 2022; revised 15 July 2022; accepted 16 July 2022; published 20 October 2022

The polarized photoluminescence from atomically thin transition metal dichalcogenides is a frequently applied tool to scrutinize optical selection rules and valley physics, yet it is known to sensibly depend on a variety of internal and external material and sample properties. In this work, we apply combined angle- and polarization-resolved spectroscopy to explore the interplay of excitonic physics and phenomena arising from the commonly utilized encapsulation procedure on the optical properties of atomically thin $MoSe_2$. We probe monolayers prepared in both suspended and encapsulated manners. We show that the hBN encapsulation significantly enhances the linear polarization of exciton photoluminescence emission at large emission angles. This degree of linear polarization of excitons can increase up to ∼17% in the hBN encapsulated samples. As we confirm by finite-difference time-domain simulations, it can be directly connected to the optical anisotropy of the hBN layers. In comparison, the linear polarization at finite exciton momenta is significantly reduced in a suspended $MoSe_2$ monolayer, and becomes notable only in cryogenic conditions. This phenomenon strongly suggests that the effect is rooted in the k-dependent anisotropic exchange coupling inherent in 2D excitons. Our results have strong implications on further studies on valley contrasting selection rules and valley coherence phenomena using standard suspended and encapsulated samples.

https://doi.org/10.1364/OPTICA.464533

1. INTRODUCTION

Polarization-dependent photoluminescence (PL) spectroscopy has been widely applied as a powerful tool to enhance our understanding of the optical properties of collective excitations in atomically thin semiconductors [1–4]. The canonical locking of spin and valley degrees of freedom manifests in significant degrees of circular polarization of the exciton PL [5–7], and valley coherent superpositions can be studied via the linearly polarized exciton emission [8–10]. However, in most works, a large numerical aperture setup is applied, which collects a significant range of emission angles and exciton momenta and thus probes a nonnegligible part of the excitonic dispersion relation. In this work, we address the consequences of collecting large momentum excitons in the optical spectroscopy of two-dimensional (2D) semiconductors.

First, our study focuses on the optical response of a suspended $MoSe_2$ monolayer, since the exciton response will be determined mostly by the internal bandstructure [11–14]. There, the valley exchange coupling is predicted to yield two orthogonally polarized, frequency-split exciton bands, which are frequently referred to as TE and TM exciton dispersion [11,15–18]. While this momentum-dependent polarization splitting has been invoked to explain phenomena including the valley depolarization of excitons in transition metal dichalcogenides (TMDCs) [15,19,20], to the best of our knowledge, its direct spectral features have been obscured thus far by experimental limitations. In this regard, our observation of the onset of a momentum-dependent linear exciton polarization at cryogenic temperatures is a first strong signature for the direct manifestation of the exciton exchange splitting.

Second, our study explores the angle-dependent polarized PL of a $MoSe_2$ monolayer encapsulated by hexagonal boron nitride (hBN), which is also a van der Waals layered material with a bandgap $E_g \sim 6$ eV [21–23]. This huge gap makes it applicable for many ultraviolet photonic and optoelectronic applications [24–29]. In the last decade of flourishing developments of 2D quantum materials, hBN has also been exhaustively used in constructing high-quality van der Waals heterostructures [30]. For example, hBN capping can protect environment-sensitive 2D magnetic materials from degradation [31], yield unprecedented carrier mobility in graphene [32], and also form periodic moiré lattices with graphene due to the crystallographically compatible lattices [33]. The hBN encapsulation of TMDC monolayers also leads to much reduced excitonic linewidths that approach the homogeneous limit [34], which makes it much easier to identify the exciton fine structures and excited states [14,35–37].

The advantages of integrating hBN into heterostructures stem from its chemical inertness, mechanical stability, commensurate lattices with other 2D materials, and homogeneous dielectric protections due to its atomically flat interfaces [38]. However, much less attention has been paid to the effects of its dielectric anistropy on the optical properties of van der Waals heterostructures. Our study reveals that the use of hBN flakes to encapsulate the TMDC monolayer of $MoSe_2$ has a significant impact on the polarization properties of TMDC exciton emissions as revealed via far-field angle-resolved PL measurements.

2. CONCEPTS AND EXPERIMENTAL PRINCIPLES

The linearly polarized excitonic orientation in TMDC monolayers results from long-range exchange interaction, which mixes the circularly polarized valley excitons and yields two new linearly polarized eigenstates, i.e., TE and TM excitons [11,15–17]. The exchange interaction and TE-TM mode splitting increase as a function of the exciton in-plane wave vector. However, only a small population of excitons, namely, those whose in-plane wave vectors lie within the radiative light cone, can couple to light and be measured [39]; see Fig. 1(a). As compared to the conventional III-V semiconductor quantum wells, although both the direct and exchange Coulomb interactions are enhanced due to the much reduced dielectric screening in these 2D limited monolayer crystals [40–43], the TE-TM splitting within the light cone is rather small compared to the exciton linewidth [44]. hBN encapsulation can reduce the inhomogeneous broadening, but it is also expected to increase the screening between charges and reduce the amplitude of exchange interactions [16]. In terms of measuring the TE and TM excitons, polarization measurements at high wave vectors thus seem more feasible than unpolarized spectroscopic measurements of the TE-TM splitting [19].

In the case of far-field polarization- and angle-resolved PL measurements, the projection of the emission wave vector in the monolayer plane is equal to the exciton wave vector. The relationship between the emission angle θ and exciton wave vector "k" can be expressed as

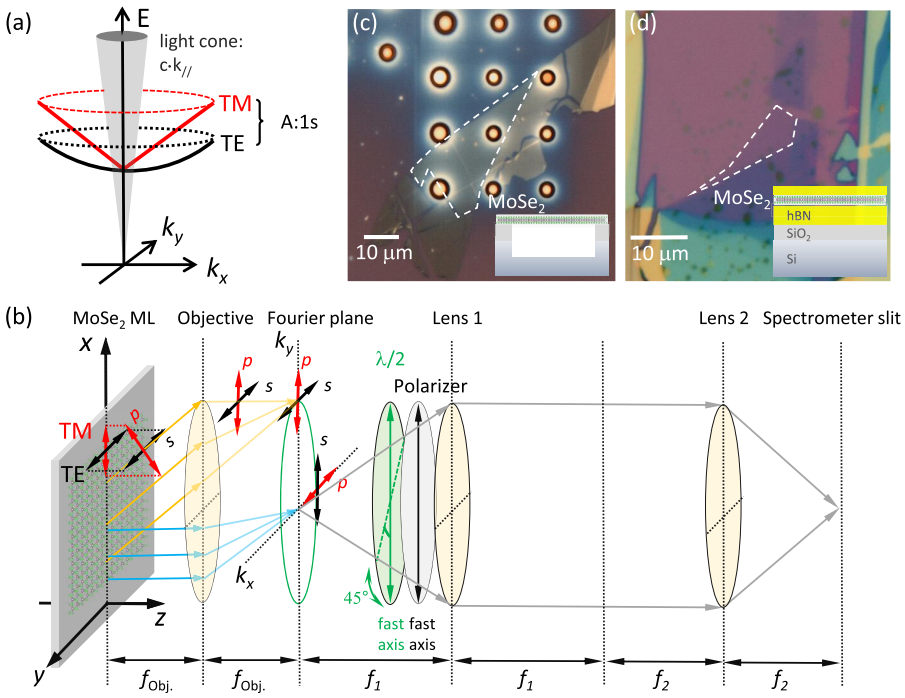

Fig. 1. Polarization-resolved momentum-space imaging and sample structures. (a) TE-TM dispersions of A:1s excitons in an excitonic quasi-particle picture. Close to the light cone, TM excitons have a linear dispersion relation, lying energetically higher than the TE excitons that have a parabolic dispersion [11]. The light cone is shown as the shaded grey area. (b) Back focal plane imaging setup. Following radiative recombination of the exciton in a $MoSe_2$ monolayer, the emitted photons are collected by an objective with an effective focal length $f_{Obj.} = 4$ mm, and NA = 0.42, which corresponds to a maximum half collection angle $\theta = 25°$. The back focal plane of the objective corresponds to the momentum space. The s- and p-polarized components coming respectively from the TE and TM excitons can then be selected by the following half wave plate and linear polarizer. The polarized back focal plane is then focused by two additional lenses on the slit of the spectrometer and imaged onto a CCD detector. The focal length $f_{1(2)}$ of lens 1(2) is 50 (40) cm. (c) Microscope image of sample 1: $MoSe_2$ monolayer (in white dashed contour) suspended over a hole (depth of 1 μm and diameter of 3 μm) in the hole arrays with 15 μm spacing. (d) Microscope image of sample 2: hBN encapsulated $MoSe_2$ monolayer (in white dashed contour) on a SiO_2 (100 nm)/Si wafer. The insets of (c) and (d) illustrate the sample structures.

$$k = \frac{2\pi}{\lambda} \sin\theta, \tag{1}$$

where λ is the emission wavelength. Figure 1(b) illustrates our experimental geometry where the TE and TM excitons are associated with the *s*- and *p*-polarization detection geometry, respectively. From a classical perspective, the *s*-polarized emission is entirely determined by the TE excitons whose motion is perpendicular to the dipole orientation. In contrast, the detected *p*-polarized emissions come from the projection of the TM excitons onto the monolayer plane. TM excitons therefore have the center-of-mass momenta along their dipole axis.

3. RESULTS AND DISCUSSION

A. Sample Structures

Our study is conducted primarily on two samples; see Figs. 1(c) and 1(d). Sample 1 is a $MoSe_2$ monolayer suspended on a hole (depth of 1 μm and diameter of 3 μm). The array of holes with 15 μm spacing is milled by a focused ion beam into a SiO_2 (100 nm)/Si wafer. Sample 2 is a $MoSe_2$ monolayer encapsulated by hBN and deposited on the SiO_2 (100 nm)/Si wafer. The thicknesses of the top and bottom hBN flakes are measured using atomic force microscopy as 6.7 ± 2.0 nm and 258.1 ± 3.3 nm, respectively [see fabrication details in Supplement 1, Section 1]. Raman scattering measurements of both samples can be found in Supplement 1, Section 5. The samples are mounted on the cold finger of a closed-cycle cryostat with a tunable temperature range from 10 to 293 K.

B. Optical Microscopy Measurements

The excitation for PL microscopy is a 532 nm continuous wave laser, which is focused by the objective to a 2 μm spot. We first use the binning mode of the spectrometer and disperse the PL emission. In both samples, the wavelength of the A:1s exciton PL redshifts with increasing temperature [see Figs. 2(a) and 2(d)]. At 10 K, the full width at half maximum of the A:1s exciton PL emission is 2.3 (9.7) meV in sample 2 (1), which is consistent with the narrowing effects induced by hBN encapsulation [34]. We then use edge filters to filter out only the A:1s exciton peak for further angle-resolved PL measurements.

Our setup has a maximum half collection angle of 25° that is determined by a long working distance objective (NA = 0.42) outside the cryostat windows. The back focal plane of the objective, i.e., the Fourier plane, carries the angle or momentum information of the luminescence [see Fig. 1(b)]. The acquired momentum space thus has the circular shape of the rear aperture of the objective. The emission into the largest angle corresponds to the maximum detectable in-plane exciton momentum, and the emission normal to the monolayer plane is centered on the center of the Fourier plane. The Fourier plane is then focused on the spectrometer slit by two additional lenses and then imaged onto the CCD detector to extract the exciton PL emission in momentum space. Note that we use zero order of the spectrometer grating to acquire the entire undispersed momentum-space PL of A:1s excitons.

To perform linearly polarized detection, we use a combination of a half-wave plate and a linear polarizer. The transmission axis of the polarizer is aligned along the spectrometer slit to maintain the efficiency of the optical detection. The half-wave plate between the linear polarizer and the objective's back focal plane also has its fast axis aligned to the spectrometer slit. We can rotate the fast axis of the half-wave plate by 45° to switch the optical detection between orthogonal linear polarizations, i.e., selecting either the TE (*s*-polarized) or TM (*p*-polarized) exciton mode. Four exemplary *s*- and *p*-polarized momentum-space radiation patterns of A:1s, excitons in samples 1 and 2 at 10 K are shown in Figs. 2(b), 2(c), 2(e), and 2(f). The degree of linear polarization (DOLP) is then calculated as

$$\mathrm{DOLP} = \frac{I_s - I_p}{I_s + I_p}, \tag{2}$$

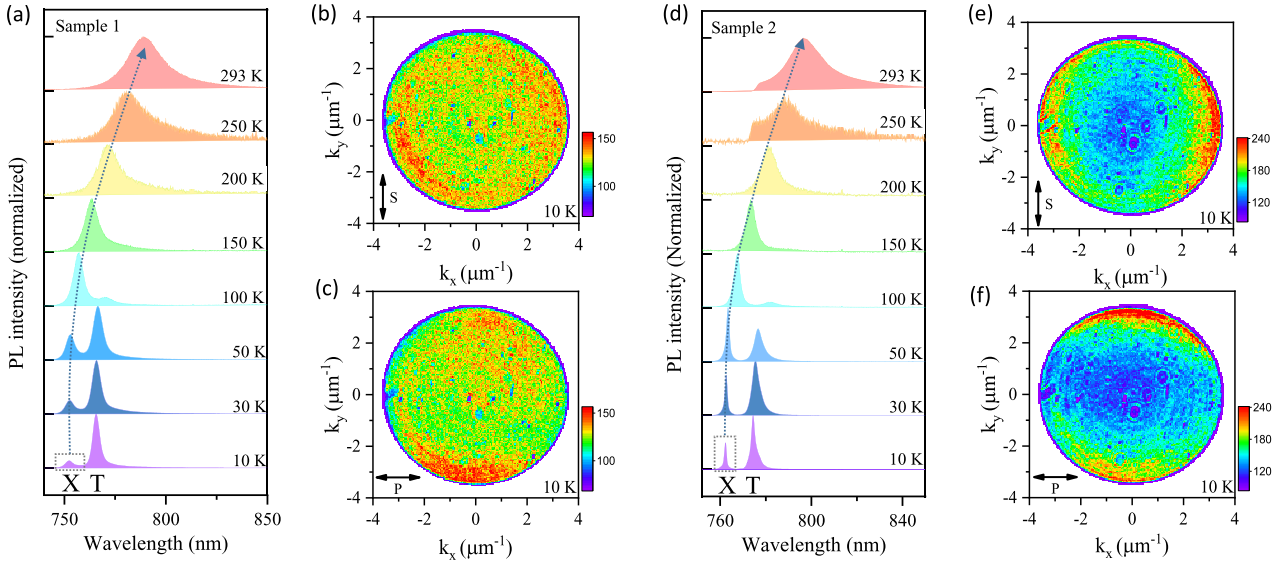

Fig. 2. Real- and momentum-space PL. Dispersed and binned real-space temperature-dependent PL of (a) sample 1 and (d) sample 2. X and T labels denote the A:1s exciton and trion, respectively. Undispersed momentum-space PL imaging of (b) TE and (c) TM excitons in sample 1 at 10 K, and (e) TE and (f) TM excitons in sample 2 at 10 K. These emission maps correspond to the A:1s exciton PL peaks marked by the dashed frames in (a) and (d). The arrows represent the linear polarization of the emission. The false-color scale bars represent the PL counts on each CCD pixel.

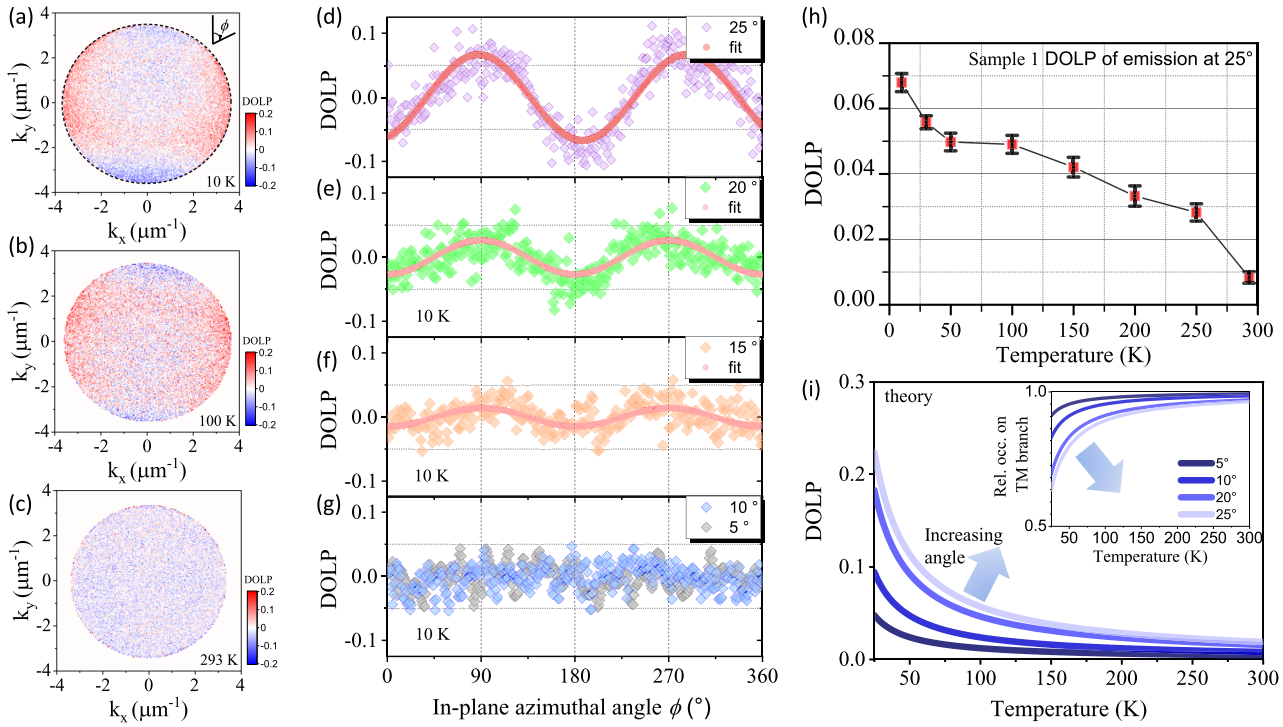

Fig. 3. DOLP of A:1s exciton PL in momentum space of sample 1 and simulations. (a)–(c) Temperature-dependent DOLP at 10 K, 100 K, and 293 K. The scale bar is linear with red (blue) colors marking positive (negative) values. The white parts with a scale of zero correspond to unpolarized emission regions in momentum space. (d)–(g) DOLP values in (a) at different emission angles of 25°, 20°, 15°, 10°, and 5°, which correspond to pixels on the circular data-extraction paths with radii of in-plane wave vectors of 3.51 μm^{-1} [dashed circle in (a)], 2.85 μm^{-1}, 2.15 μm^{-1}, 1.44 μm^{-1}, and 0.72 μm^{-1}, respectively. Dataset of 360 azimuthal angles (ϕ) are extracted for each selected emission angle. (h) Temperature dependence of the fitted DOLP amplitudes at emission angle of 25°. The error bars represent uncertainty from the fit procedure. (i) Calculations of the temperature-dependent DOLP that considers a fully thermalized exciton distribution. The inset shows the relative occupation of A:1s excitons on the TM branch.

where I_s and I_p are the s- and p-polarized PL intensities on each CCD pixel, respectively, i.e., the PL intensity at each wave vector (k_x, k_y).

In Fig. 3(a), the DOLP diagram [calculated using the data from Figs. 2(b) and 2(c)] of the freestanding $MoSe_2$ monolayer at 10 K explicitly shows the linearly polarized emission pattern in momentum space. By using off-resonant pumping well above the single-particle bandgap, we ensure that both exciton dispersion branches are populated. Clearly, the amplitude of DOLP increases with momentum and reaches maximum value at the largest emission angle. We convert (k_x, k_y) into polar coordinates and extract a DOLP dataset of 360 equally spaced pixels on circular paths [dashed circle in Fig. 3(a)] with different radii that correspond to different emission angles θ. The data are shown in Figs. 3(d)–3(g) and Fig. S2. We then use a sine function to fit the fluctuating DOLP amplitudes as a function of the azimuthal angle (see details in Supplement 1). The amplitudes of the fitted DOLP of sample 1 at 10 K are 0.067 (25°), 0.05 (22.5°), 0.027 (20°), 0.018 (17.5°), and 0.014 (15°). The DOLP pattern starts to flatten out for emission angles below 10°, and the amplitudes cannot be fitted out of the noise level anymore. We attribute this k-dependent increase of polarization to the fact that the splitting between TE and TM excitons monotonically increases with momentum, and thus the relative population between these branches should also encounter a scaling with k.

It is also evident from Figs. 3(b) and 3(c) that the amplitude of the DOLP drops with rising temperature and totally smears out at a room temperature of 293 K, where the thermal activation of excitons to higher energy and momentum states is much more efficient, yielding an approximately equalized population of TE- and TM-exciton branches. Figure 2(h) summarizes the fitted temperature-dependent modulation of the DOLP amplitude at the maximum collection angle, which decreases monotonically and totally diminishes at 293 K.

To give further evidence for this conclusion, we consider a thermal Boltzmann distribution $f_\eta(\theta, T)$ of A:1s excitons on TE and TM branches and calculate the PL intensity of each branch by using the Elliot formula [45]

$$I_\sigma(\theta, \omega, T) = \frac{2}{\hbar}\sum_\eta \mathrm{Im}\left[\frac{f_\eta(\theta, T)|M^{\sigma,\omega}_{\theta,\eta}|^2}{\mathcal{E}^\eta_\theta - \hbar\omega - i(\gamma^\eta_\theta + \Gamma^\eta_\theta(T))}\right]. \quad (3)$$

Here, $\sigma = s, p$ represents the polarization indices, $\mathcal{E}^\eta_\theta$ is the exciton resonant energy with η being the branch index of TE-TM excitons, $M^{\sigma,\omega}_{\theta,\eta}$ is the angle-dependent optical matrix element, and γ^η_θ and Γ^η_θ are the radiative decay rate and phonon scattering rate, respectively. Then we use Eq. (2) to calculate the DOLP and summarize the results in Fig. 3(i). The calculated DOLP increases at high emission angles and low temperatures, which well captures the qualitative trend in the temperature-dependent experiment. However, the overestimation of the DOLP amplitude for low temperatures ($T < 100$ K) in the Elliot model is probably due to significant deviation of the exciton distribution in the realistic sample from the thermalized Boltzmann model assumed above. The inset of Fig. 3(i) also shows the calculated relative occupation between TM and TE branches, which converges to one as the

temperature increases. The occupations converge more rapidly at lower measurement angles, as the splitting between the two branches is smaller. Thus, the agreement between experiment and theory is a strong indicator that the DOLP patterns of sample 1 at a low temperature indeed result from the branch splitting of TE-TM excitons induced by the exchange coupling.

As shown in Fig. 2(d), the encapsulation of the $MoSe_2$ monolayer yields a substantial narrowing in its emission linewidth. To assess its impact on PL polarization, we also plot in Figs. 4(a)–4(c), the experimental results of the temperature-dependent DOLP of sample 2 with the hBN encapsulated $MoSe_2$ monolayer. Surprisingly, we find that the fitted amplitude of DOLP at the maximum emission angle is as high as ∼17% at 10 K and reduces only slightly with rising temperature [see Fig. 4(c)]. Indeed, the amplitude drop of the DOLP in sample 2 has a smaller amplitude of only ∼2% [see fitting results in Fig. S3(a)], which is in stark contrast to the much stronger decline ∼6% in sample 1. This is a clear sign that the dielectric screening effects, induced by hBN encapsulation, significantly suppress the exchange interactions in the TMDC monolayer.

The general enhancement of DOLP of exciton emission at high angles is a direct consequence of the optical properties of the hBN flakes in the van der Waals heterostructure: the low index layer surrounding the active material effectively forms a cavity-like structure, which impacts the light–matter coupling of TMDC excitons. We argue that the strongly anisotropic dielectric properties of hBN, with refractive indices of 1.58 and 2.25, respectively, for polarization parallel and perpendicular to the c axis are the main cause for the very different DOLP properties of the encapsulated sample. Due to this birefringence, the TE and TM excitons couple differently to the surrounding dielectric resonator, and this increases the TE-TM splitting and, thus, enhances the DOLP. Since this effect comes from the structural properties of the sample, it is not affected by the exciton distribution and therefore does not reduce with temperature. Hence, an intrinsic ∼15% DOLP pattern at the maximum collection angle can still survive up to room temperature. We will show in the following section that the experimental results on samples 2 are indeed consistent with finite-difference time-domain (FDTD) simulations of the far-field emission pattern that explicitly take the in-plane and out-of-plane refractive indices of hBN into account.

C. Finite-Difference Time-Domain Simulations

A sketch of the setup of the 2D FDTD simulation of sample 2 is shown in Fig. 4(d). The $MoSe_2$ monolayer is embedded in hBN where the top hBN layer has a fixed thickness of 10 nm. The refractive index of the $MoSe_2$ monolayer is taken from Ref. [46]. The thickness of the bottom hBN layer is varied between 250 and 260 nm. The entire van der Waals heterostructure is placed on a SiO_2 (100 nm)/Si substrate. Perfectly matched layer boundary conditions are applied to all boundaries of the simulation box, which has a width of 20 μm and a height of 3.8 μm. A broadband dipole source is used to impulsively excite the sample. The dipole axis is rotated by 45° around the z axis. A field monitor is placed 600 nm above the sample surface and collects the emitted and reflected, time-averaged fields. To account for the anisotropy of hBN, its anisotropic, complex refractive index, taken from Ref. [47], is incorporated into the FDTD simulations. To simulate the cavity-like effect on the DOLP observed in the experiments, the electric field components E_s and E_p are recorded as a function of the emission angle θ. The field components are recorded at a wavelength of 800 nm, which is quite close to the exciton PL wavelength at 796.5 nm in sample 2 at room temperature [see Fig. 2(d)]. From these quantities, the DOLP is calculated according to Eq. (2), where $I_p = |E_p|^2$ and $I_s = |E_s|^2$.

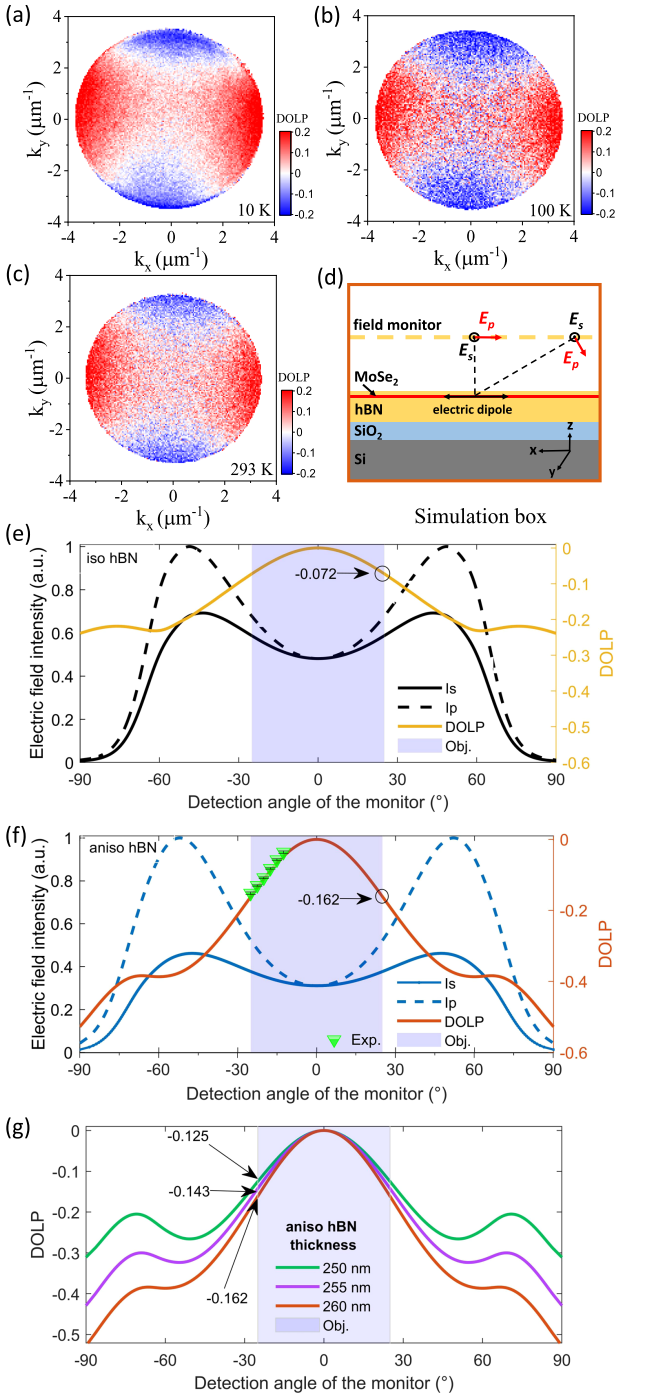

Fig. 4. DOLP of A:1s exciton PL in momentum space of sample 2 and FDTD simulations. (a)–(c) Experimental results of the temperature dependence of DOLP at 10 K, 100 K, and 293 K. The scale bar is the same as in Figs. 3(a)–3(c). (d) Structural setup of sample 2. FDTD simulations of $I_s = |E_s|^2$ and $I_p = |E_p|^2$, and DOLP at far field using (e) isotropic and (f) anisotropic hBN refractive indices. The shaded areas in the middle signify the maximum collection angle of the objective. (g) Comparison of DOLP as a function of the bottom hBN thickness (250 nm, 255 nm, and 260 nm), using anisotropic refractive indices.

Figures 4(e) and 4(f) compare the FDTD simulation results using the isotropic and anisotropic refractive indices of the bottom hBN layer with the same thickness of 260 nm. The electric field intensities are all normalized to $|E_s|^2$. We can see that the relative amplitude of $|E_p|^2$ differs in the isotropic and anisotropic cases of the hBN layer, which is reasonable since the real part of the out-of-plane refractive index $n_\perp = 1.58$ is significantly smaller than the in-plane component $n_\parallel = 2.25$. In the isotropic case, the DOLP has an amplitude of 0.072 at 25° (maximum collection angle of our setup); however, it is increased to 0.162 when simulated with the anisotropic refractive index of hBN. The calculated DOLP as a function of the emission angle is perfectly consistent with the six fitted experimental values shown as green triangles in Fig. 4(f). These values are fitted based on the data from Fig. 4(c) [see details in Supplement 1, Fig. S3]. Using the anisotropic refractive index of hBN, in Fig. 4(g), we also calculate the DOLP as a function of the bottom hBN thickness. When the thickness is reduced, the amplitude of the DOLP also decreases, which signifies the detuning effects when varying the cavity length (see also Supplement 1, Section 6 for the FDTD simulations of the averaged field intensities in the real space for 250 nm and 260 nm bottom hBN thicknesses).

4. SUMMARY

By using angle-resolved PL microscopy, we explicitly measured a maximum ∼6% linear polarization of TE-TM excitons in a free-standing $MoSe_2$ monolayer. The temperature and k-dependent polarization result from the excitonic fine structure caused by the inherent exchange interactions in TMDCs. We also elucidate a pronounced effect of a hBN capping layer cavity on linear polarization of the heterostructure, which is dominated by the intrinsic optical birefringence (anisotropy) of hBN. The much enhanced DOLP ∼17% in a hBN-encapsulated $MoSe_2$ monolayer barely changes with temperature, and it is perfectly consistent with our FDTD simulations of the layered sample structure. Our findings provide additional insights of the polarization properties of the 2D van der Waals heterostructure, and will further facilitate the future optoelectronic applications and quantum photonic devices based on 2D materials that exploit their polarization properties.

Funding. Deutsche Forschungsgemeinschaft (DFG) (SPP 2244, SCHN 1376 11-1, 14-1, SFB 1083); European Union's Horizon 2020 Research and Innovation Program (881603); University of Oldenburg; Bundesministerium für Bildung und Forschung (BMBF) (NanoMatFutur FKZ: 13N13637); U.S. Department of Energy; Basic Energy Sciences; Division of Materials Sciences and Engineering (SC0020653); Applied Materials Inc.; National Science Foundation (DMR 2206987, CMMI-1933214, ECCS 2052527, DMR 2111812); Volkswagen-Stiftung (SMART); Japan Society for the Promotion of Science (KAKENHI) (19H05790, 20H00354, 21H05233).

Acknowledgment. B.H. and C.S. gratefully acknowledge funding by the DFG. J.T and E.M. acknowledge funding from the DFG, and the European Union's Horizon 2020 research and innovation program (Graphene Flagship). S.S and M.S. thank the BMBF for a personal research grant "Photonic Transistors" in the NanoMatFutur program. M.E. acknowledges funding by the University of Oldenburg through a Carl-von-Ossietzky Young Researchers' fellowship. S.T. acknowledges the research supported by the U.S. Department of Energy, Office of Basic Energy Sciences, Division of Materials Sciences and Engineering, Applied Materials Inc. (crystallography), NSF. C.L. acknowledges funding by Volkswagen-Stiftung (SMART). K.W. and T.T. acknowledge support from JSPS.

Disclosures. The authors declare no conflicts of interest.

Data availability. Data underlying the results presented in this paper are not publicly available at this time but may be obtained from the authors upon reasonable request.

Supplemental document. See Supplement 1 for supporting content.

REFERENCES

1. G. Wang, A. Chernikov, M. M. Glazov, T. F. Heinz, X. Marie, T. Amand, and B. Urbaszek, "Colloquium: excitons in atomically thin transition metal dichalcogenides," Rev. Mod. Phys. **90**, 021001 (2018).
2. J. A. Schuller, S. Karaveli, T. Schiros, K. He, S. Yang, I. Kymissis, J. Shan, and R. Zia, "Orientation of luminescent excitons in layered nanomaterials," Nat. Nanotechnol. **8**, 271–276 (2013).
3. M. Brotons-Gisbert, R. Proux, R. Picard, D. Andres-Penares, A. Branny, A. Molina-Sánchez, J. F. Sánchez-Royo, and B. D. Gerardot, "Out-of-plane orientation of luminescent excitons in two-dimensional indium selenide," Nat. Commun. **10**, 3913 (2019).
4. N. Lundt, Ł. Dusanowski, E. Sedov, P. Stepanov, M. M. Glazov, S. Klembt, M. Klaas, J. Beierlein, Y. Qin, S. Tongay, M. Richard, A. V. Kavokin, S. Höfling, and C. Schneider, "Optical valley hall effect for highly valley-coherent exciton-polaritons in an atomically thin semiconductor," Nat. Nanotechnol. **14**, 770–775 (2019).
5. D. Xiao, G.-B. Liu, W. Feng, X. Xu, and W. Yao, "Coupled spin and valley physics in monolayers of MoS_2 and other group-vi dichalcogenides," Phys. Rev. Lett. **108**, 196802 (2012).
6. X. Xu, W. Yao, D. Xiao, and T. F. Heinz, "Spin and pseudospins in layered transition metal dichalcogenides," Nat. Phys. **10**, 343–350 (2014).
7. K. F. Mak, K. He, J. Shan, and T. F. Heinz, "Control of valley polarization in monolayer MoS_2 by optical helicity," Nat. Nanotechnol. **7**, 494–498 (2012).
8. M. M. Glazov, E. L. Ivchenko, G. Wang, T. Amand, X. Marie, B. Urbaszek, and B. Liu, "Spin and valley dynamics of excitons in transition metal dichalcogenide monolayers," Phys. Status Solidi B **252**, 2349–2362 (2015).
9. G. Wang, X. Marie, B. Liu, T. Amand, C. Robert, F. Cadiz, P. Renucci, and B. Urbaszek, "Control of exciton valley coherence in transition metal dichalcogenide monolayers," Phys. Rev. Lett. **117**, 187401 (2016).
10. A. M. Jones, H. Yu, N. J. Ghimire, S. Wu, G. Aivazian, J. S. Ross, B. Zhao, J. Yan, D. G. Mandrus, D. Xiao, W. Yao, and X. Xu, "Optical generation of excitonic valley coherence in monolayer WSe_2," Nat. Nanotechnol. **8**, 634–638 (2013).
11. D. Y. Qiu, T. Cao, and S. G. Louie, "Nonanalyticity, valley quantum phases, and lightlike exciton dispersion in monolayer transition metal dichalcogenides: theory and first-principles calculations," Phys. Rev. Lett. **115**, 176801 (2015).
12. C. Robert, T. Amand, F. Cadiz, D. Lagarde, E. Courtade, M. Manca, T. Taniguchi, K. Watanabe, B. Urbaszek, and X. Marie, "Fine structure and lifetime of dark excitons in transition metal dichalcogenide monolayers," Phys. Rev. B **96**, 155423 (2017).
13. J. Echeverry, B. Urbaszek, T. Amand, X. Marie, and I. C. Gerber, "Splitting between bright and dark excitons in transition metal dichalcogenide monolayers," Phys. Rev. B **93**, 121107 (2016).
14. G. Berghäuser and E. Malic, "Analytical approach to excitonic properties of MoS_2," Phys. Rev. B **89**, 125309 (2014).
15. M. M. Glazov, T. Amand, X. Marie, D. Lagarde, L. Bouet, and B. Urbaszek, "Exciton fine structure and spin decoherence in monolayers of transition metal dichalcogenides," Phys. Rev. B **89**, 201302 (2014).
16. J. J. Thompson, S. Brem, H. Fang, C. Antón-Solanas, B. Han, H. Shan, S. P. Dash, W. Wieczorek, C. Schneider, and E. Malic, "Valley-exchange coupling probed by angle-resolved photoluminescence," Nano. Horiz. **7**, 77–84 (2022).
17. F. Wu, F. Qu, and A. H. Macdonald, "Exciton band structure of monolayer MoS_2," Phys. Rev. B **91**, 075310 (2015).
18. T. Deilmann and K. S. Thygesen, "Finite-momentum exciton landscape in mono-and bilayer transition metal dichalcogenides," 2D Mater. **6**, 035003 (2019).
19. L. M. Schneider, S. S. Esdaille, D. A. Rhodes, K. Barmak, J. C. Hone, and A. Rahimi-Iman, "Optical dispersion of valley-hybridised coherent excitons with momentum-dependent valley polarisation in monolayer semiconductor," 2D Mater. **8**, 015009 (2020).
20. M. Selig, F. Katsch, S. Brem, G. F. Mkrtchian, E. Malic, and A. Knorr, "Suppression of intervalley exchange coupling in the presence of

momentum-dark states in transition metal dichalcogenides," Phys. Rev. Res. **2**, 023322 (2020).
21. G. Cassabois, P. Valvin, and B. Gil, "Hexagonal boron nitride is an indirect bandgap semiconductor," Nat. Photonics **10**, 262–266 (2016).
22. B. Huang, X. Cao, H. Jiang, J. Lin, and S.-H. Wei, "Origin of the significantly enhanced optical transitions in layered boron nitride," Phys. Rev. B **86**, 155202 (2012).
23. X. Blase, A. Rubio, S. G. Louie, and M. L. Cohen, "Quasiparticle band structure of bulk hexagonal boron nitride and related systems," Phys. Rev. B **51**, 6868 (1995).
24. Y. Kubota, K. Watanabe, O. Tsuda, and T. Taniguchi, "Deep ultraviolet light-emitting hexagonal boron nitride synthesized at atmospheric pressure," Science **317**, 932–934 (2007).
25. K. Watanabe, T. Taniguchi, T. Niiyama, K. Miya, and M. Taniguchi, "Far-ultraviolet plane-emission handheld device based on hexagonal boron nitride," Nat. Photonics **3**, 591–594 (2009).
26. B. Arnaud, S. Lebègue, P. Rabiller, and M. Alouani, "Huge excitonic effects in layered hexagonal boron nitride," Phys. Rev. Lett. **96**, 026402 (2006).
27. C. Maestre, Y. Li, V. Garnier, P. Steyer, S. Roux, A. Plaud, A. Loiseau, J. Barjon, L. Ren, and C. Robert, "From the synthesis of hBN crystals to their use as nanosheets in van der Waals heterostructures," 2D Mater. **9**, 035008 (2022).
28. S. Roy, X. Zhang, A. B. Puthirath, *et al.*, "Structure, properties and applications of two-dimensional hexagonal boron nitride," Adv. Mater. **33**, 2101589 (2021).
29. G. Cassabois, G. Fugallo, C. Elias, P. Valvin, A. Rousseau, B. Gil, A. Summerfield, C. Mellor, T. Cheng, L. Eaves, C. T. Foxon, P. H. Beton, M. Lazzeri, A. Segura, and S. V. Novikov, "Exciton and phonon radiative linewidths in monolayer boron nitride," Phys. Rev. X **12**, 011057 (2022).
30. A. K. Geim and I. V. Grigorieva, "Van der Waals heterostructures," Nature **499**, 419–425 (2013).
31. B. Huang, G. Clark, D. R. Klein, D. MacNeill, E. Navarro-Moratalla, K. L. Seyler, N. Wilson, M. A. McGuire, D. H. Cobden, D. Xiao, W. Yao, P. Jarillo-Herrero, and X. Xu, "Electrical control of 2D magnetism in bilayer CrI_3," Nat. Nanotechnol. **13**, 544–548 (2018).
32. L. Wang, I. Meric, P. Huang, Q. Gao, Y. Gao, H. Tran, T. Taniguchi, K. Watanabe, L. Campos, D. Muller, J. Guo, P. Kim, J. Hone, K. L. Shepard, and C. R. Dean, "One-dimensional electrical contact to a two-dimensional material," Science **342**, 614–617 (2013).
33. C. R. Dean, L. Wang, P. Maher, C. Forsythe, F. Ghahari, Y. Gao, J. Katoch, M. Ishigami, P. Moon, M. Koshino, T. Taniguchi, K. Watanabe, K. L. Shepard, J. Hone, and P. Kim, "Hofstadter's butterfly and the fractal quantum Hall effect in moiré superlattices," Nature **497**, 598–602 (2013).
34. F. Cadiz, E. Courtade, C. Robert, G. Wang, Y. Shen, H. Cai, T. Taniguchi, K. Watanabe, H. Carrere, D. Lagarde, M. Manca, T. Amand, P. Renucci, S. Tongay, X. Marie, and B. Urbaszek, "Excitonic linewidth approaching the homogeneous limit in MoS_2-based van der Waals heterostructures," Phys. Rev. X **7**, 021026 (2017).
35. B. Han, C. Robert, E. Courtade, M. Manca, S. Shree, T. Amand, P. Renucci, T. Taniguchi, K. Watanabe, X. Marie, L. E. Golub, M. M. Glazov, and B. Urbaszek, "Exciton states in monolayer $MoSe_2$ and $MoTe_2$ probed by upconversion spectroscopy," Phys. Rev. X **8**, 031073 (2018).
36. C. Robert, B. Han, P. Kapuscinski, A. Delhomme, C. Faugeras, T. Amand, M. R. Molas, M. Bartos, K. Watanabe, T. Taniguchi, B. Urbaszek, M. Potemski, and X. Marie, "Measurement of the spin-forbidden dark excitons in MoS_2 and $MoSe_2$ monolayers," Nat. Commun. **11**, 4037 (2020).
37. M. Goryca, J. Li, A. V. Stier, T. Taniguchi, K. Watanabe, E. Courtade, S. Shree, C. Robert, B. Urbaszek, X. Marie, and S. A. Crooker, "Revealing exciton masses and dielectric properties of monolayer semiconductors with high magnetic fields," Nat. Commun. **10**, 4172 (2019).
38. A. Raja, L. Waldecker, J. Zipfel, Y. Cho, S. Brem, J. D. Ziegler, M. Kulig, T. Taniguchi, K. Watanabe, E. Malic, T. F. Heinz, T. C. Berkelbach, and A. Chernikov, "Dielectric disorder in two-dimensional materials," Nat. Nanotechnol. **14**, 832–837 (2019).
39. X. Marie and B. Urbaszek, "Ultrafast exciton dynamics," Nat. Mater. **14**, 860–861 (2015).
40. A. Chernikov, T. C. Berkelbach, H. M. Hill, A. Rigosi, Y. Li, O. B. Aslan, D. R. Reichman, M. S. Hybertsen, and T. F. Heinz, "Exciton binding energy and nonhydrogenic Rydberg series in monolayer WS_2," Phys. Rev. Lett. **113**, 076802 (2014).
41. M. Bayer, G. Ortner, O. Stern, A. Kuther, A. Gorbunov, A. Forchel, P. Hawrylak, S. Fafard, K. Hinzer, T. Reinecke, S. N. Walck, J. P. Reithmaier, F. Klopf, and F. Schäfer, "Fine structure of neutral and charged excitons in self-assembled In(Ga)As/(Al)GaAs quantum dots," Phys. Rev. B **65**, 195315 (2002).
42. L. C. Andreani and F. Bassani, "Exchange interaction and polariton effects in quantum-well excitons," Phys. Rev. B **41**, 7536 (1990).
43. E. Hanamura, "Rapid radiative decay and enhanced optical nonlinearity of excitons in a quantum well," Phys. Rev. B **38**, 1228 (1988).
44. H. Fang, B. Han, C. Robert, M. Semina, D. Lagarde, E. Courtade, T. Taniguchi, K. Watanabe, T. Amand, B. Urbaszek, M. M. Glazov, and X. Marie, "Control of the exciton radiative lifetime in van der Waals heterostructures," Phys. Rev. Lett. **123**, 067401 (2019).
45. S. Brem, A. Ekman, D. Christiansen, F. Katsch, M. Selig, C. Robert, X. Marie, B. Urbaszek, A. Knorr, and E. Malic, "Phonon-assisted photoluminescence from indirect excitons in monolayers of transition-metal dichalcogenides," Nano Lett. **20**, 2849–2856 (2020).
46. Y. Li, A. Chernikov, X. Zhang, A. Rigosi, H. M. Hill, A. M. Van Der Zande, D. A. Chenet, E.-M. Shih, J. Hone, and T. F. Heinz, "Measurement of the optical dielectric function of monolayer transition-metal dichalcogenides: MoS_2, $MoSe_2$, WS_2, and WSe_2," Phys. Rev. B **90**, 205422 (2014).
47. A. Segura, L. Artús, R. Cuscó, T. Taniguchi, G. Cassabois, and B. Gil, "Natural optical anisotropy of hBN: highest giant birefringence in a bulk crystal through the mid-infrared to ultraviolet range," Phys. Rev. Mater. **2**, 024001 (2018).